Three-Terminal Perovskite/Silicon Tandem Solar Cells with Top and Interdigitated Rear Contacts

Philipp Tockhorn[1†*], Philipp Wagner[1,3†], Lukas Kegelmann[2], Johann-Christoph Stang[1], Mathias Mews[1], Steve Albrecht[2,4] & Lars Korte[1*]

[1] Helmholtz-Zentrum Berlin, Institute Silicon Photovoltaics, Berlin, 12489, Germany
[2] Helmholtz-Zentrum Berlin, Young Investigator Group Perovskite Tandem Solar Cells, Berlin, 12489, Germany
[3]HTW Berlin, University of Applied Sciences, Berlin, 12459, Germany
[4]Technische Universität Berlin, Fakultät IV - Elektrotechnik und Informatik, Berlin, 10587, Germany
† these authors contributed equally

*correspondence: philipp.tockhorn@helmholtz-berlin.de, korte@helmholtz-berlin.de,

Abstract

We present a three-terminal (3T) tandem approach for the interconnection of a perovskite top cell with an interdigitated back contact (IBC) silicon heterojunction (SHJ) bottom cell. The general viability of our cell design is further verified with drift-diffusion simulations indicating efficient charge carrier transport throughout the whole device and an efficiency potential of ≈27% using readily available absorber and contact materials. Our experimental proof-of-concept device reaches a combined PCE of 17.1% when both subcells are operating at their individual maximum power point. To emulate different operation conditions, the current–voltage characteristics of both cells were obtained by measuring one subcell while the other cell was set to a fixed bias voltage. Only a slight mutual dependence of both subcells was found. As determined by electrical simulations, it likely stems from the resistance of the electron contact on the cell's rear side, which is shared by both subcells. The optimisation of this contact turns out to be a major design criterion for IBC 3T tandems. We demonstrate that our current proof-of-concept cells are limited by this series resistance as well as by optical losses, and we discuss pathways to approach the simulated efficiency potential by an optimised device design.

KEYWORDS: Tandem Solar Cell, Perovskite, Silicon Heterojunction, Three-Terminal, Perovskite-Silicon Tandem, Interdigitated Back Contact

Introduction

Silicon represents the predominant material for solar cell fabrication with 95% market share in 2017[1]. Its efficiency potential is close to the optimum predicted by the Shockley-Queisser (SQ) detailed balance limit for a single semiconductor solar cell, resulting in an efficiency potential of slightly above 30%[2], and 29.56%[3] if Auger recombination is taken into consideration. With Kaneka's back contacted silicon heterojunction (SHJ) solar cells recently achieving 26.7%[4], this efficiency potential is almost entirely exploited as recognised by the same authors in a previous publication[5]. Thus, efficiencies well above 30% can only be achieved by combining multiple semiconductors with different band gaps in a tandem architecture, either monolithically in a two-terminal (2T) device or, electrically decoupled, in a four terminal (4T) approach. Despite achieving high efficiencies[6–9], tandem devices based on costly III–IV semiconductors (GaAs, GaInP) are not able to compete with the much more cost-effective silicon-based single-junction solar cells[10].

A new perspective on solar tandem applications has risen from the emergence of perovskite solar cells in recent years. On a timescale of less than a decade, the power conversion efficiencies (PCEs) of solar cells based on metal halide perovskites have reached remarkable efficiencies up to 25.2%[11], thus outperforming other thin film technologies such as CIGS or CdTe[4]. The outstanding optoelectronic properties together with the flexibility in absorber composition as well as facile and potentially cost-effective fabrication routes make metal halide perovskites promising candidates for tandem applications with Si bottom cells.

The band gap of crystalline silicon is close to the optimum value for a bottom cell in a two-semiconductor tandem device[12] while the band gap of the perovskite top cell is in the range of 1.5–1.6 eV for the best single-junction solar cells[13, 14] and can be adjusted close to the top cell optimum of about 1.7 eV[15]. Recently, there have been several scientific reports on perovskite/silicon-based 2T[15, 16, 17, 18, 19] and 4T tandem[20, 21] devices with record efficiencies of 28.0% and 26.7% respectively, thus surpassing that of the world-record silicon single-junction solar cell. These enhancements were achieved among others by changing the polarity to p-i-n top cells with less parasitic absorption, carefully adjusting the optics of the tandem stack, introducing protective buffer

layers and tailoring the perovskite's band gap. Further improvements of the fabrication procedure are expected to yield PCEs above 30% for both the 2T and 4T tandem design[16, 22, 23].

Both tandem device designs have advantages but also drawbacks: in a 2T tandem solar cell, the fabrication route is rather straightforward. The monolithic design omits lateral charge transport through absorptive transparent conductive oxide (TCO) layers between the subcells and in the field only a single inverter is required. On the other hand, the total current density is limited by the subcell yielding the lower current. Hence, the optical design of such a device requires careful tuning to achieve ideal current matching between the subcells[24]. Since the amount of light reaching each subcell changes with daytime, weather conditions, and illumination angle, a lab-optimised 2T tandem device might still suffer from reduced energy yield due to current mismatch in a real-world application. In comparison, 4T tandem solar cells do not require current matching, grant a higher flexibility in material choice, but the necessity of two individual substrates, additional transparent conductive layers and complex interconnection are major challenges of this approach.

In contrast to these more common approaches, three-terminal (3T) tandems feature a contact that is shared by both subcells, allowing for the individual operation of both subcells in a monolithic device with a single substrate, thus combining the characteristic advantages of the more common architectures: a 3T tandem is a monolithic device and thus, the predicted combined photogenerated current density[25] under AM1.5G conditions is expected to be the similar as in state of the art 2T tandems[16, 19] as the employed layer stack is almost identical to that of a 2T tandem. Moreover, electrically, the subcells can be operated independently at their maximum power point (MPP) in the 3T device, resembling the 4T tandem case[26], which makes it more robust against varying spectra. Also, note that recently a neat module integration of 3T tandems has been suggested by interconnecting the subcells such that the number of required inverters is the same as for 2T[27]. One possible 3T configuration which was initially proposed by Sakai and Umeno[28] features the third terminal at the recombination layer in between the subcells. Multiple experimental realisations of this 3T design were reported for different absorber layer combinations such as InGaAs/InP[29], GaAs/Si[30] and recently perovskite/silicon[31]. However, a 3T cell in such configuration inevitably leads to parasitic absorption within the relatively thick (> 100 nm) middle contact. Thus, a more favourable approach comprises a back contacted bottom

cell (IBC 3T) as initially proposed by Nagashima *et al.*[32] and schematically sketched in the inset of Fig. 1. Being a rather unconventional configuration, the number of published studies is fairly limited. Recently, several theoretical and experimental reports on the accurate operation of 3T devices and the expected interplay between the subcells have been published: a GaInP and Si cell wired in quasi 3T configuration was experimentally[26] and theoretically[33, 34] reported, and more recently, a 3T IBC of individually fabricated GaInP and Si cells was realised by bonding the subcells with transparent conductive adhesive[35]. Additionally, the influence of different top cell currents injected into an interdigitated back contact (IBC) cell on its power output was experimentally evaluated and it was found that the combined power output of the 3T tandem is independent of the amplitude of the top cell's current[36]. Regarding 3T perovskite/silicon tandem solar cells featuring an interdigitated back contact, so far only theoretical reports focusing on the electrical properties of a nanostructured top contact [37] and optical[25] properties exist but to our knowledge no report of an experimental realisation. Here, after briefly assessing the limiting efficiencies of the different tandem configurations in a simulation study, we report on the first experimental realisation of a back contacted 3T device combining perovskite and silicon subcells in a monolithic device followed by an in-depth analysis of optical and electrical limitations and potentials.

Results

Simulation of Limiting Efficiencies

To illustrate inherent performance differences between the investigated tandem designs , we perform detailed balance calculations similar to the procedure reported by de Vos[12] (cf. SI for details). We make the assumption that a 4T tandem inevitably requires two middle TCO layers for lateral charge transport. In our simulations, we use indium tin oxide (ITO) films with a combined thickness of 300 nm which is in the range of typical TCO thicknesses for the middle contacts of such devices. We assume that the only optical difference between 3T and 4T device is the parasitic absorption in these additional ITO layers which we calculate from Lambert-Beer's law and optical data reported elsewhere[38]. Note that a) any other optical changes such as differing reflectivity are neglected in this simplified model, and b) other contact geometries are conceivable, e.g. thinner TCOs, which would lead to higher transparency

but would – assuming unchanged TCO resistivity – require metal grid fingers, yielding shadowing losses. Nevertheless, the current losses discussed in the following are expected to be of the correct order of magnitude. The limiting PCEs of 2T, 3T and 4T tandem devices as a function of the perovskite's band gap along with schematic drawings of each approach are displayed in Figure 1 and the values obtained for 2T and 4T agree well with literature[39]. Due to current matching constraints, the 2T configuration has a narrow region for the perovskite's band gap to yield highest PCEs with a maximum of 45.1%. In contrast, 3T and 4T applications both allow for high PCEs over a broader top cell band gap region. Here, the 3T configuration yields a slightly higher maximum PCE (45.3% vs. 44.5%) under the chosen assumptions because of the missing middle TCO and thus a decreased parasitic absorption.

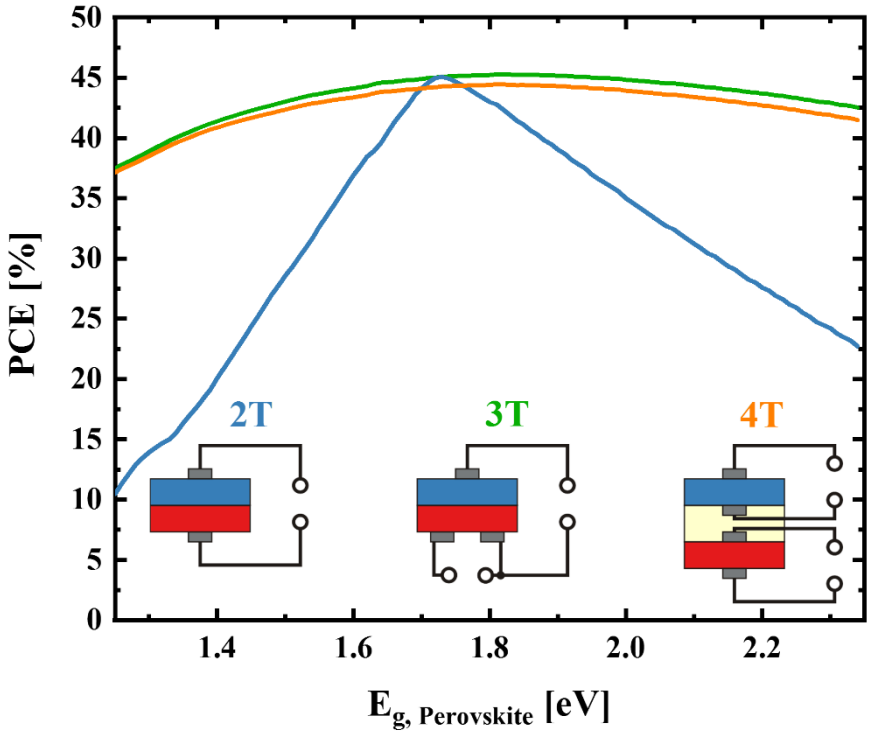

Figure 1: Calculated tandem solar cell PCEs of 2T, 3T, and 4T tandem device designs as a function of the perovskite top cell's band gap based on detailed balance calculations as described in the text and SI. As a bottom cell material, silicon with E_g=1.12 eV was selected. The schematic drawings (blue for perovskite, red for silicon, interconnection layers for the 4T approach are depicted in yellow, contact grid fingers in grey; note that the latter are not implied within the model, but are needed for a real-world application and are therefore depicted here) represent the simplified device layouts of the 2T, 3T and 4T approaches.

IBC 3T Tandem Device Design and Fabrication

The device layout and operating principle of our experimentally realised perovskite/silicon IBC 3T device with an n-i-p perovskite top cell are schematically displayed in Figure 2a: electrons and holes generated by NIR photons in the Si bottom cell are collected by the respective IBC contacts as indicated by the dashed arrows. Electrons being generated from visible photons in the perovskite top cell pass into

the Si through the n-type layers that interconnect the subcells, to be likewise collected by the n-contact of the IBC cell as indicated by the solid arrow pointing downward in Fig 2a). On the other hand, the corresponding holes that are generated in the perovskite subcell are electrically blocked by the n-type interconnection layer and are extracted at the top contact through a hole transport layer (HTL) and a TCO (indicated by the upward solid arrow in Figure 2a).

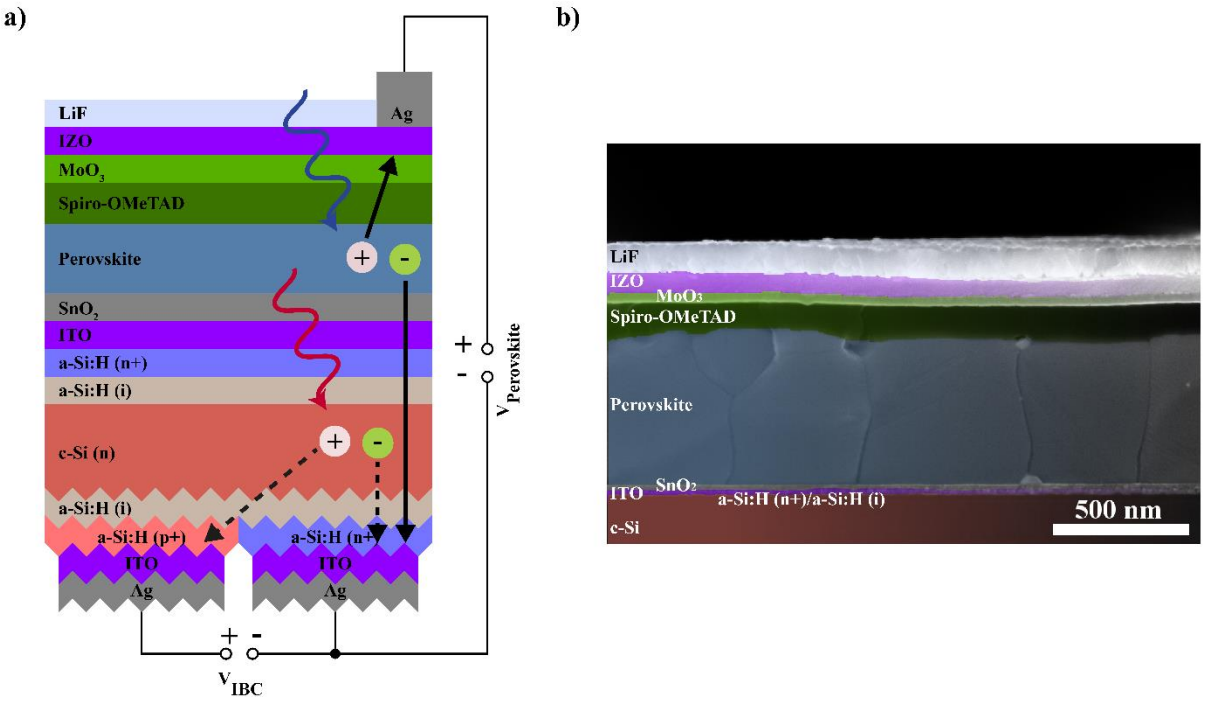

Figure 2: a) Schematic drawing (not to scale) of our IBC 3T tandem solar cell and its operating principle. The structural drawing includes all used layers. b) SEM micrograph of the perovskite top cell and interconnection layers of the presented device.

The experimentally realised layer stack of an IBC 3T tandem device is schematically depicted in Figure 2a. As a basis for the IBC 3T device, we use an IBC SHJ solar cell with polished front and textured rear sides. Note, that this is different from the usual, optically more favourable IBC single junction cell design comprising a textured front side with a-Si:H(i)/SiN_X surface passivation/antireflective coating[40]: the flat surface is mandatory since the herein used spincoated layers of the perovskite top cell can coat nano-structured surfaces[41] but not the typically used random pyramids with sizes in the range of, in our case, 1–2 µm. The IBC SHJ's front side is coated with an a-Si:H(i)/nc-Si:H(n)/ITO layer stack with the 20 nm thick ITO layer being patterned to the same size as the rear-side active area. The nc-Si:H(n)/ITO stack used here as cell interconnection[42] was chosen to render the cell fabrication compatible with the deposition of SnO_2, which was optimised for the growth on ITO. Several such devices have been processed per wafer and were subsequently separated by laser

cutting for further processing. Figure 2b shows a SEM micrograph of the perovskite top cell and the interfacial region to the IBC SHJ bottom cell. For the top cell's fabrication, a 30 nm thick layer of SnO_2 as electron transport layer (ETL), a mixed-cation lead mixed-halide ($Cs_{0.05}(FA_{0.83}MA_{0.17})_{0.95}Pb(I_{0.83}Br_{0.17})_3$) perovskite absorber[43] with a bandgap of 1.63 eV (layer thickness ca. 550 nm) and a 110 nm thick layer of doped Spiro-OMeTAD as HTL are spincoated on top of the individual IBC cells. The semi-transparent top contact is realised with a 75 nm thick layer of indium zinc oxide (IZO) which is sputtered on a 35 nm evaporated molybdenum oxide (MoO_3) buffer layer which protects the HTL from sputter damage[44]. The cell is finished by evaporating a silver frame around the edges of the top IZO, thereby defining a designated illumination area[45] of 0.78 cm². As a last step, a 115 nm thick lithium fluoride (LiF) film is thermally evaporated on the active area. A detailed description of the fabrication procedure can be found in the Device Fabrication Details section.

Electronic Characterisation of IBC 3T Tandems

Subsequently, we measured the individual current–voltage (J–V) characteristics of perovskite and IBC SHJ cells in as-fabricated devices under AM1.5G light conditions. For an exact determination of the IBC 3T PCE it is necessary to measure both subcells simultaneously as the exact distribution of currents generated in the subcells is governed by Kirchhoff's law[36]. To this end, top and bottom cell were connected to two source measure units (SMUs) sharing the same ground potential. It is connected to the IBC SHJ's n-contact, which also serves as the perovskite cell's electron contact (cf. Figure 2a). This configuration allows for measuring both cells simultaneously and to examine the mutual influence of the subcells under different bias conditions. The combined effective PCE of the IBC 3T device results from a simultaneous measurement of both subcells at their MPP. Figure 3a presents J-V characteristics of perovskite and IBC SHJ subcell at this working point while the respective other cell is held at MPP. For the IBC SHJ with the incoming AM1.5 illumination filtered by the perovskite top cell, a PCE of 5.4% was measured whereas the best PCE of the perovskite cell was at 12.3% in the reverse scan (for other characteristic performance parameters see Table 1). The effective PCE of the IBC 3T device is 17.1% as determined from the simultaneous MPP tracking of both subcells displayed in Figure 3b. Here, the IBC SHJ contributing 5.4% and the perovskite 11.7%, owing to a slightly hysteretic behaviour.

Table 1: Measured device parameters of the perovskite and IBC SHJ subcells in an IBC 3T tandem device.

	Direction	V_{oc} (V)	J_{sc} (mA/cm^2)	*FF* (%)	η_{J-V} (%)	η_{MPP} (%)
Perovskite	$V_{oc} \rightarrow J_{sc}$	1.117	17.4	63.5	12.3	11.7
	$J_{sc} \rightarrow V_{sc}$	1.104	17.3	57.5	11.0	
IBC SHJ		0.600	14.4	64.2	5.5	5.4
				Σ	17.8	**17.1**

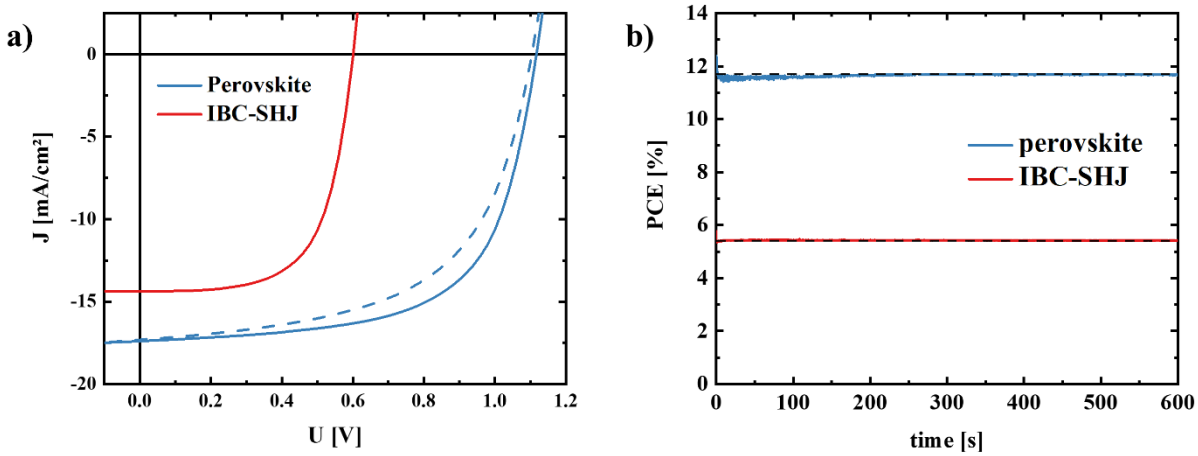

Figure 3: Effective Performance of the best IBC 3T device: a) J–V characteristics of the IBC 3T tandem with the perovskite top (blue) and IBC SHJ bottom (red) cell. For these measurements, the other subcell was set to MPP. For the perovskite top cell in the IBC 3T configuration, both a forward (dashed) and a reverse (solid) scan are displayed. b) simultaneous MPP tracked PCE of perovskite and IBC SHJ subcell.

Moreover, we characterise the effect of different voltage conditions on both subcells. To this end, one of the subcells is set to a fixed bias voltage whilst the other is characterised, i.e. J–V scanned or MPP tracked. By varying the bias voltage setting, also the current extracted through the common n-contact is altered, which in turn leads to a change in Ohmic losses over the series resistance of this terminal. Besides the MPP bias conditions (circles, opaque), Figure 4a and b also display the J–V characteristics of both perovskite and IBC SHJ subcell when the respective other cell is set to J_{sc} (squares, transparent) or V_{oc} (triangle, transparent) conditions. With increasing voltage in the biased perovskite subcell (i.e. reduced current extraction), the J–V characteristics of the measured IBC SHJ subcell improve. For the opposite case, i.e. biasing the IBC SHJ and measuring the J–V characteristics of the perovskite subcell, this trend is more pronounced, possibly owing to ion movements within the perovskite occurring on longer time scales than the J–V scanning that are superimposed on the bias-induced changes. When biasing the perovskite (IBC SHJ) subcell and tracking the MPP of the IBC SHJ (perovskite) subcell for 100 s at each bias (see Figure S3), the same reduction in performance is observed in the MPP tracked subcell as shown in Figure 4c and d: for the IBC SHJ, the performance reduction reaches almost 0.4%$_{abs}$ whereas it is only 0.25%$_{abs}$ for the perovskite.

In addition, to examine the effect of the perovskite cell's presence and, if occurring, any degradation due to perovskite cell processing on the photovoltaic performance of the IBC SHJ cell, we measured the J–V characteristics of the IBC SHJ before processing the top cell on it (see Figure S1 and Table S1) as well as the performance of a semi-transparent perovskite single-junction cell processed with Spiro-OMeTAD/MoO_3/IZO top contact in the same run (see Figure S2 and Table S2). As expected, when integrated into the IBC 3T tandem, the IBC SHJ shows a strongly reduced J_{sc} due to the filtering effect and reflection losses, which are imposed by the top cell's layer stack. Moreover, $V_{oc,IBC}$ is reduced by 79 mV and FF_{IBC} by 2.5%$_{abs}$. Apart from the lower illumination intensity, this reduction in $V_{oc,IBC}$ is also caused by a limitation of our current cell design: while the bottom cell size is 1 cm², the opening in the metal frame of the perovskite cell's top contact is only 0.78 cm². Thus, a significant portion of the silicon cell's active device area is now shaded, forming a parasitic diode, which reduces $V_{oc,IBC}$ through additional recombination[46]. The observed drop in FF_{IBC} can also be explained by this shading. Within our current IBC design, the outer fingers are always part of the bottom cell's emitter. It is well known, that a partially shaded emitter has a significant impact on the *FF* of IBC solar cells[47]. Therefore, avoiding such shading is an important design criterion and is planned in the future by either adapting the bottom cell's layout or the top cell's metallisation design. It is, thus, no inherent flaw of the 3T concept itself but only of our current design.

The perovskite cell behaves more robustly upon tandem cell integration: for the semi-transparent perovskite single-junction cells, we observe a comparable hysteretic behaviour and similar V_{oc}s as for the top cell in the IBC 3T device. Note that the single junction cells are illuminated through the ITO/SnO_2 layers, which yields higher J_{sc}s than illuminating through the rather absorptive front layer stack in the IBC 3T. The similar J–V behaviour of the perovskite single junction cells in comparison with the IBC 3T case indicates that the latter architecture does not impose fundamental performance limitations on the perovskite top cell.

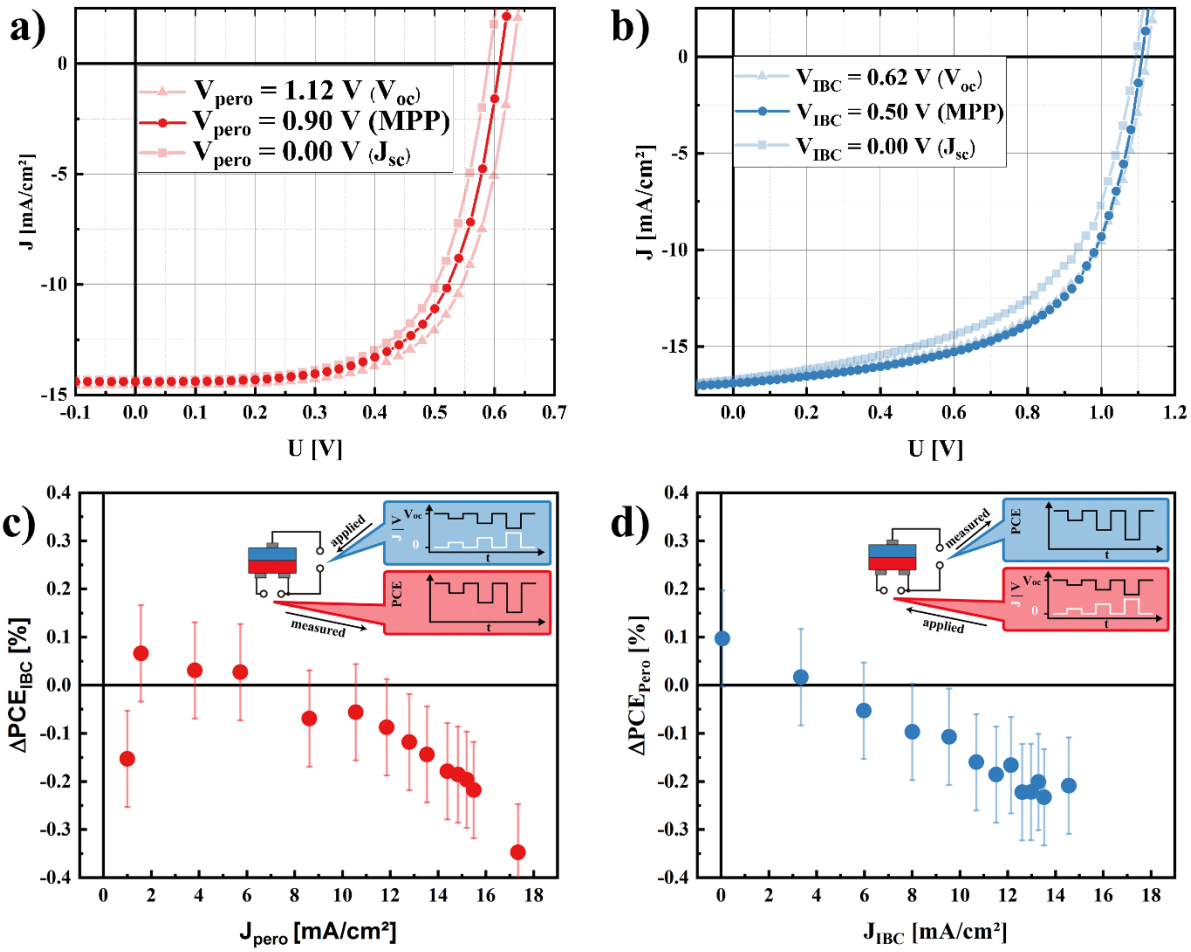

*Figure 4: Top: J–V characteristics of a) IBC SHJ and b) perovskite subcell while the respective other subcell is set to a certain bias. Bottom: change of MPP-tracked PCE of c) IBC SHJ and d) perovskite plotted against the current density generated at a certain bias in the respective other subcell. The insets in c) and d) illustrate the bias configuration of perovskite and IBC SHJ cell where "applied" refers to setting a fixed bias to one subcell and "measured" refers to the detection of the second subcell's response in the MPP signal. The error bars in c) and d) are set to 0.1 % accounting for a drift observed in the experiment (see Figure S3***Fehler! Verweisquelle konnte nicht gefunden werden.****).*

Optical Characterisation of IBC 3T Tandems

To investigate the optical losses in the IBC 3T device, EQE measurements of both subcells were conducted (Figure 5a) and supplemented with optical simulations (cf. Optical Modelling section). From the measured EQE spectra, we obtained EQE-integrated J_{sc} values of $J_{sc,Pero}$ = 17.32 mA/cm² and $J_{sc,IBC}$ = 13.65 mA/cm² which are in good agreement with the values determined from J–V characteristics (17.4/17.3 and 14.4 mA/cm², respectively). Here, $J_{sc,Pero}$ agrees very well with the value obtained from J–V characterisation. For $J_{sc,IBC}$, there is a discrepancy of about 0.7 mA/cm² between J–V- and EQE-derived values. We attribute this behaviour mostly to the reduced minority carrier lifetime at low minority carrier densities (see Figure S4b) determined on the IBC SHJ's wafer prior to metallisation. To illustrate the impact of this dependence, we carried out measurements with and without

bias-illuminated bottom cell (see Figure S4a) and the non-measured cell held floating (i.e. V_{oc} conditions). For both subcells, the bias illumination leads to higher J_{sc}s. In particular, $J_{sc,IBC}$ suffers from a lack of bias illumination with a significantly reduced value of 10.17 mA/cm² (instead of 13.65 mA/cm² with bias illumination) whereas for the perovskite the J_{sc} increases from 16.79 mA/cm² to 17.32 mA/cm² under bias illumination. Furthermore, the optical reflection of our IBC 3T devices was measured to assess the contribution of optical losses. Combining these reflection measurements with the EQE under bias-illumination (Figure 5a) illustrates reflection losses of 4.25 mA/cm² at the front side. This can be ascribed to flat interfaces within the device as well as thin-film interferences which are clearly visible (e.g. at approximately 800 nm) and have a considerable share in these reflection losses. Moreover, there are 10.96 mA/cm² internal losses in the device's bulk which arise from parasitic absorption in contact layers and non-unity internal quantum efficiencies (IQE) of the absorbers. We mostly attribute these losses in our non-optimised cells to a strong absorption occurring at the MoO_3/IZO interface: for MoO_3, it was previously demonstrated that sputter depositing metal oxides atop can chemically reduce the MoO_3 and thereby induce a broadband absorption[48]. Moreover, there is additional parasitic absorption expected stemming from the IZO and Spiro-OMeTAD as seen in similar devices reported previously[49].

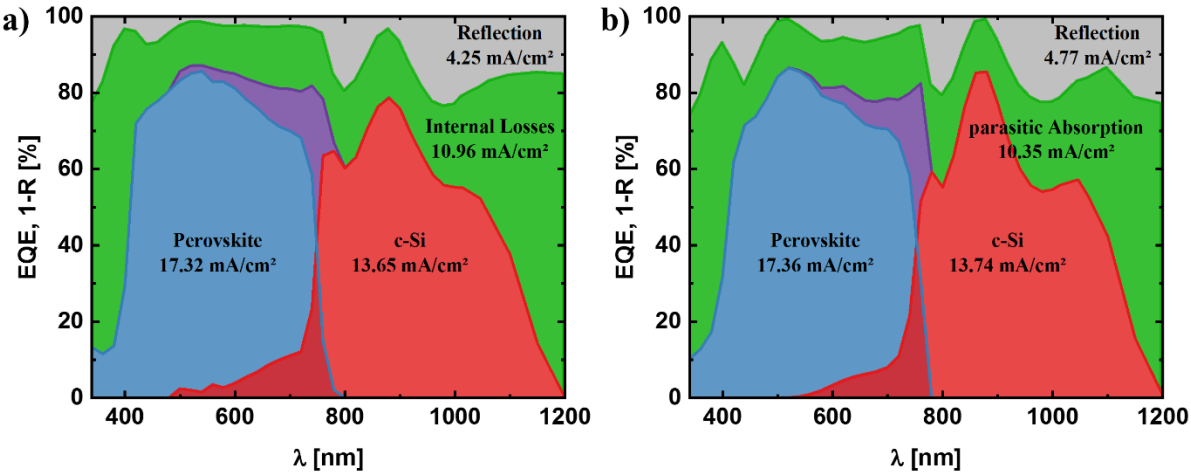

Figure 5: a) Measured, b) Simulated EQE of perovskite and IBC SHJ subcell, internal losses (parasitic absorption and collection losses) and reflection of the best IBC 3T device.

Modelling

Optical Modelling

In a next step, we conducted optical simulations of the IBC 3T tandem cell stack with the MATLAB-based programme GenPro4[50, 51]; details can be found in the SI. To account for the strong absorption in the MoO_3 layer, we adjusted the optical extinction coefficient, *k*, to reproduce the measured absorbance, using calculations based on Lambert-Beer's law (see Figure S5). With this adjustment, we were able to obtain a reasonable agreement with the measured EQE and reflection data (Figure 5b). The simulated layer thicknesses and equivalent current absorbed in the individual layers are given in Table S11. As expected, a large contribution of the parasitic absorption can be ascribed to the front IZO (0.75 mA/cm³) and MoO_3 (6.52 mA/cm²) and a smaller yet still significant portion to absorption in the Spiro-OMeTAD (1.86 mA/cm²). As seen in previous studies on 2T tandems[24], it should be possible to overcome these optical limitations with a suitable choice of contact materials and film thicknesses.

Verification of Efficient Charge Transport in IBC 3T Devices using Sentaurus TCAD

As seen in Figure 4a and Table 1, the performance of our experimentally realised IBC 3T cell is further limited by the low *FF*s of both cells as well as the decreased $V_{oc,IBC}$. To assess if these limitations are of a fundamental nature or merely due to the shortcomings in our current experimental procedures, we first carry out drift-diffusion simulations with Sentaurus TCAD. In the following section, we assess whether these results, obtained using the full physical picture of the semiconductor equations, can be described in terms of the usual elements of solar cell equivalent circuits, i.e. diodes and resistors.

For the electric parameters of the individual layers, we adopted values reported elsewhere[47, 52] and implemented slight modifications to obtain solar cell parameters similar to the single junction champion cells processed in our institute, which will be further discussed in the next section. The simulated solar cell parameters are displayed in Table S3. These values agree reasonably well with literature reports for both perovskite[53] and IBC SHJ[54]. For more details, we refer to the Sentaurus TCAD Simulation Details section in the SI.

In order to reach sufficient electron selectivity between the two subcells in a tandem device, the ETL adjacent to the perovskite must create an asymmetric energetic barrier[34] (see Figure 6a and b): The

conduction band only experiences a small band offset, thus allowing electrons to pass[55] while holes are blocked by the considerable energetic barrier in the valence band. The simulated solar cell parameters for both subcells when set to MPP conditions in the IBC 3T configuration are included in Table S4. With respect to the IBC SHJ solar cell, the perovskite cell merely acts as a filter layer resulting in less light reaching the c-Si absorber (in particular when held at $V_{oc,Pero}$ conditions). Consequently, the simulated $J_{sc,IBC}$ and $V_{oc,IBC}$ decrease (-21.6 mA/cm² and -35 mV, respectively), while there is a slight increase in *FF* (+1.2 $\%_{abs}$). In contrast, the effect of adding an entire wafer cell to the n-contact of the perovskite cell may be expected to have a significant impact as electrons generated in the perovskite layer must pass through the entire wafer to be extracted from the solar cell. However, it turns out that this effect is rather marginal in the simulation: although the wafer is expected to increase the series resistance contribution of the n-contact as already stated above, the simulated *FF* of the perovskite top cell drops by only 0.2%$_{abs}$ and $V_{oc,Pero}$ is reduced by 3.3 mV when both subcells are under MPP conditions, which may be related to the additional recombination in the SHJ cell. These results confirm the experimental indications of a mostly unaffected $V_{oc,Pero}$. Furthermore, we investigate the band diagrams under AM1.5 illumination (Figure 6a and b) when the IBC SHJ (perovskite) subcell is set to a voltage corresponding to MPP conditions while the perovskite (IBC SHJ) subcell is set to different bias conditions (J_{sc}, MPP and V_{oc}). As is evident, the band diagram in the subcell at MPP conditions is mostly unaffected by the different bias conditions of the other subcell. Investigating the interconnection region in more detail (Figure 6c and d), it appears that different bias conditions on the IBC SHJ have a stronger influence on the potential distribution of the perovskite cell. When the IBC SHJ's bias is changed from $J_{sc,IBC}$ to $V_{oc,IBC}$ conditions, a band bending (BB) change of 11.1 meV in the c-Si at the a-Si(n) interface (y = 0.000 µm) translates to a BB shift of 8.7 meV in the perovskite at the ETL interface (y = 0.045 µm). On the other hand, when changing the perovskite's bias from $J_{sc,Pero}$ to $V_{oc,Pero}$ conditions, the downward shift of 21.6 meV in the perovskite at the interface with the ETL (y = 0.045 µm) only translates to a change of 4.3 meV in the c-Si at the a-Si:H(n) interface (y = 0.000 µm). This different behaviour is caused by the different nature of the devices: in the perovskite cell, the n-i-p design together with the thin perovskite layer leads to a strong influence of changes in the applied front potential being translated into changes also at the interconnection interface. In the IBC SHJ however, the space charge

region (SCR) is located at the cell's rear within the less than 1 µm of the 250 µm absorber. Thus, changes in the applied potential on the rear contact lead to changes in the band's position which are confined mostly to this region. These results of only a slight mutual dependence of the two subcells demonstrate the general viability of the perovskite/silicon IBC 3T tandem approach and are comparable to simulations presented earlier[56]. Since Sentaurus TCAD implements resistive loss mechanisms through material parameters rather than by setting explicit values for series or shunt resistances, we further analyse our IBC 3T cell in the following section using LTspice simulations to shed light on the influence of resistive losses in IBC 3T cells.

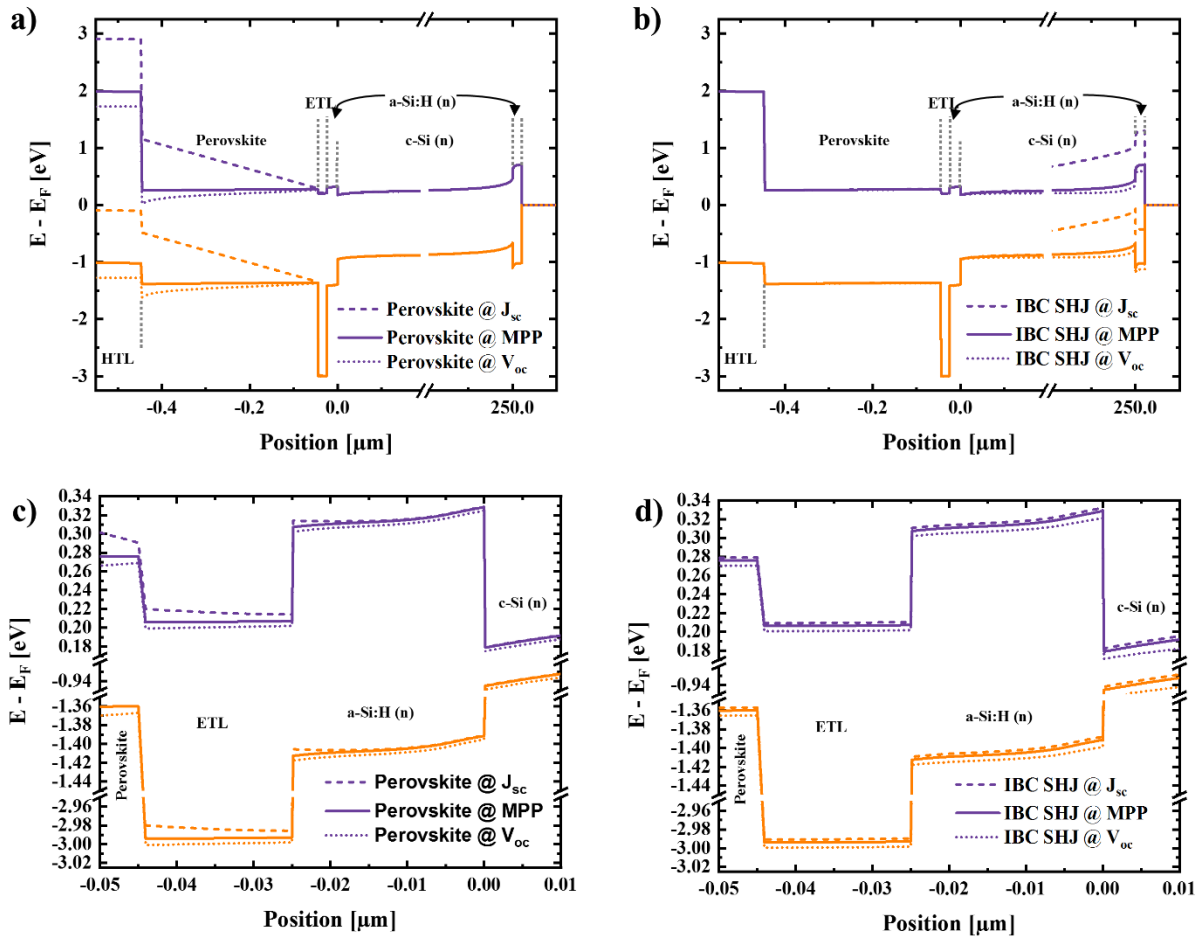

Figure 6: Sentaurus TCAD simulated band diagrams of a simplified IBC 3T tandem device structure under AM1.5 illumination. a) Perovskite is set to different bias conditions while IBC SHJ is at MPP conditions. b) IBC SHJ is set to different bias conditions while perovskite is at MPP conditions. c) zoom-in to the interconnection region of a) and d) zoom-in to the interconnection region of b). Charge carriers generated in the bottom cell are collected at their respective rear-side electrode of which only the n-contact is shown here. Note the break on the x-axis (a and b) and the multiple breaks on the y-axis (c and d).

LTspice Equivalent Circuit Simulations

To understand the experimentally observed bias-dependence of both subcells, we modelled the equivalent circuit of our IBC 3T device configuration in LTspice[57]. Figure 7 displays the electrical equivalent circuit of the device that was used for the electrical modelling and is based on one-diode models for each subcell. This equivalent circuit model is similar to the one presented by Santbergen et al[25]. Diode characteristics (i.e. the saturation current density j_0 and the parasitic resistances R_s and R_{shunt}) were obtained by fitting one-diode models to measured J–V characteristics (cf. Table S12 for details). Fit and measured data agree very well (with a slight deviation around the MPP) as shown exemplarily in Figure S7. For the simulations, the top cell's R_s and R_{shunt} as well as the bottom cell's R_{shunt} are taken as obtained from the fit. The R_s of the bottom cell is split into the contact resistance of the p-contact and the combined resistance of the n-contact and the c-Si bulk (i.e. the resistance that is shared by both subcells) following the proposed distribution in Paviet-Salomon et al.[58]. An additional interconnection resistance (R_{IC}) is added in-between both subcells, representing the interconnection layers. We see that they marginally influence only the top cell's *FF*. The impact of R_{IC} is shown in Figure 8 where its numeric value is swept within a device-relevant range. Different operating points of the subcells were simulated by adjusting the current provided by the respective current source from 0 mA (open-circuit conditions) to J_{sc} (short-circuit conditions). As in the experiment, one subcell was then swept in current whilst for the biasing subcell the voltage across its electrodes was obtained. Here, we consider two different cases: 1) an exact representation of the experimentally realised IBC 3T device, and 2) an optimised device comprising the best perovskite and SHJ IBC single-junction solar cells fabricated in our institute. The latter case is supposed to show a realistically feasible potential utilising the very layers that are used in our tandems. Note, that the currents of the single-junction devices were adjusted to an optimised current distribution as obtained by optical simulations utilising again GenPro4 (as discussed above and in the Optical Simulation Details section in the SI). Using this approach, we were able to reproduce the performance reduction mainly caused by the voltage drop at V_{oc} as also seen in our actual devices (cf. Figures SI 8 and 9). Interestingly, we were able to pinpoint the likely origin of this effect: The simulations show that it can be reproduced by increasing the shared portion of the bottom cell's series resistance, $R_{s,shared}$, alone (i.e. the resistivities of the wafer bulk and the electron contact).

Indeed, the dependence of one cell's characteristics on the operating point of the respective other cell vanishes completely when this resistance is set to zero, i.e. for the limiting case (which cannot be achieved in real world devices). At this point the two subcells become independent from each other, representing the ideal theoretical case as also discussed elsewhere[34]. Thus it can be concluded that during device fabrication utmost attention on designing this shared contact to be very lowly resistive as well as on choosing appropriate wafer material are crucial to minimize the mutual dependence of the subcells' J-V-characteristics. The tuneability of contact resistivities by means of material, layer properties, and geometry choices has been successfully shown for IBC SHJ solar cells[59]. Specifically, combined resistances of n-contact and wafer down to 0.47 Ωcm² for IBC SHJ cells[58] were reported, which indicates that $R_{s,shared}$ can be tuned to values well below 1.1 Ωcm² in our current cells.

In the optimised device case, a combined PCE of 26.9% with both subcells operating at MPP was simulated using the discussed model. Note that this value is not representing the overall PCE-potential for IBC 3T tandems and is mostly limited by the rather absorptive front contact layer stack which we also use for our experiments. Further characteristics are presented in Table 2.

Table 2: Measured solar cell parameters of the best single junction devices fabricated in our institute and modelled parameters for the optimised device case utilising this very solar cells.

	V_{oc} (V)	J_{sc} (mA/cm^2)	*FF* (%)	PCE (%)
Single Perovskite	1.172	21.1	77.4	19.8
Single IBC SHJ	0.710	41.3	78.2	22.9
3T Perovskite (modelled)	1.164	19.5	79.2	18.0
3T IBC SHJ (modelled)	0.680	15.8	83.0	8.9
			Σ_{3T}	**26.9**

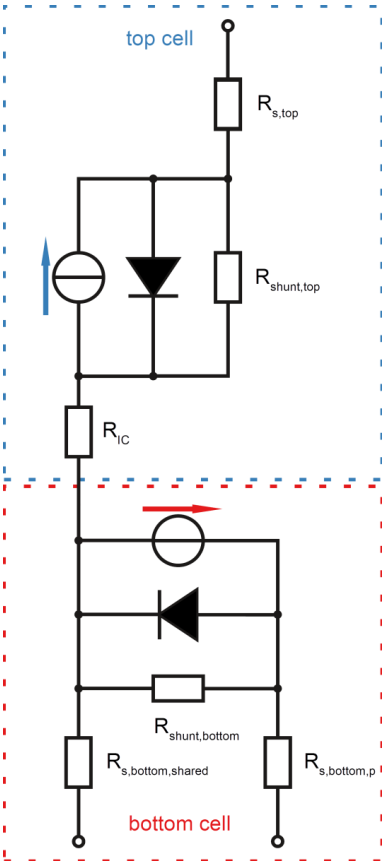

Figure 7: Equivalent electrical circuit of the IBC 3T configuration including all parameters used in the LTspice model

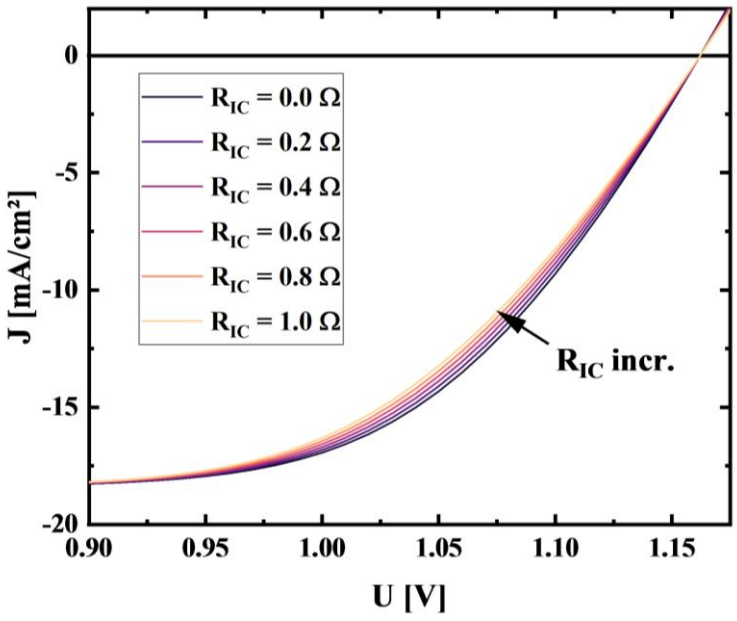

Figure 8: Influence of the R_{IC} (representing the interconnection layers) on the top cell's FF, modelled with LTspice for the optimised device case. Note that the abscissa starts at 0.9 V

In a next step, we investigated the influence of both $R_{s,shared}$ and R_{IC} (i.e. the resistances governing the mutual dependence of both subcells) on the PCE of each subcell. Results are depicted in Figure 9a–c. As discussed above, the R_{IC} mostly affects the top cell's *FF* and consequently PCE, which decreased with increased R_{IC} for a specific $R_{s,shared}$. Interestingly though, the latter has an overall larger impact on the top cell's performance due to a significant drop in $V_{oc,Pero}$ by up to 45 mV within the chosen resistance range. This drop in $V_{oc,Pero}$ does not occur for a fixed $R_{s,shared}$ and gradually increased R_{IC}. When investigating the influence of these resistances on the bottom cell (Figure 9b), it becomes evident that its PCE decreases linearly with increasing $R_{s,shared}$ and the R_{IC} does not seem to have an impact at all. This is, however, only true for properly functioning devices. If the R_{IC} is set to values in the order of kiloohms (Figure 9c), representing the case of faulty interconnection with otherwise intact subcells, PCE_{IBC} increases considerably with an increased R_{IC}, which is mainly driven by gains in $V_{oc,IBC}$ and (to a lesser extent) in FF_{IBC}. This effect is even more pronounced the larger the $R_{s,shared}$ gets because then both subcells become less independent. Although the bottom cell clearly benefits from a large R_{IC}, this is, of course, not beneficial for the overall tandem performance.

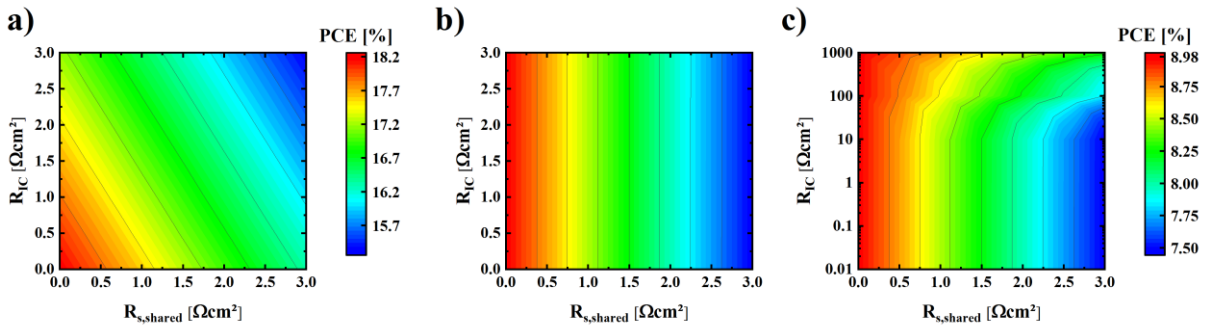

Figure 9: Simulated influence of the interconnection resistance R_{IC} and the shared portion of the bottom cell's series resistance $R_{s,shared}$ on PCE of a) the top cell and b),c) the bottom cell where in c) high R_{IC} values, representing a malfunctioning interconnection with otherwise intact subcells were simulated. Note that figures b) and c) share the same PCE colour scale on the right and all figures share the same x-axis range. These calculations were conducted for the optimised device case.

Conclusions

In conclusion, we have demonstrated the first experimental realisation of a novel three-terminal (3T) perovskite/silicon tandem solar cell with an interdigitated back contact (IBC), yielding a combined stabilised PCE of 17.1% under MPP-conditions. Furthermore, we have investigated the mutual dependence of both subcells by conducting bias-dependent J–V measurements, which show that the photovoltaic performance of both subcells is slightly reduced when changing the bias of the respective other cell from V_{oc} to J_{sc} conditions. Between these two operating points of the other cell, the performance loss amounts to $0.25\%_{abs}$ for the perovskite and $0.4\%_{abs}$ for the silicon subcell, which we attribute to the series resistance of the shared IBC SHJ's wafer bulk and n-contact. As evidenced utilising drift-diffusion simulations with realistic material's parameters, in principle the IBC 3T configuration does not significantly reduce the performance of the perovskite top cell. Also, for the IBC SHJ bottom cell, only the illumination intensity is reduced by the filtering effect of the top cell. Overall, an efficiency of 26.9% is expected for this optimised case. A detailed optoelectronic analysis revealed that the pronounced differences between the drift-diffusion simulation and our experimental proof-of-concept cell can be largely ascribed to limitations that are specific to our current non-optimised cell design: 1) optical losses due to pronounced parasitic absorption and reflection in the non-optimised front side contact layer stack, 2) probably a high series resistance $R_{s,shared}$ on the shared n-contact, and 3) partial shading of the 1 cm² active area of the IBC bottom cell by the metal frame of the top cell's front contact, which in our current design has an opening of only 0.78 cm². We have discussed pathways to overcome

these limitations by optimising or using different layers in the cell stack and by an improved geometrical design of the contact. Therefore, we consider our results a proof of concept for perovskite/silicon IBC 3T tandem solar cells with an interdigitated back contact and are confident that further optimisation of the fabrication process will allow for efficiencies in the range of state-of-the-art 2T and 4T perovskite/silicon tandem devices. We believe that the advantageous properties of the IBC 3T tandem cell concept render it an interesting alternative to the common 2T and 4T approaches. Additionally, careful optical and electrical simulations are required to evaluate the ultimate and realistically achievable efficiency potential of the different tandem architectures. This will further help to compare and assess the competitiveness of these interconnection schemes.

Device Fabrication Details

IBC SHJ subcells were built on approximately 280 µm thick 4-inch float-zone silicon wafers (front-side polished, rear-side textured, 1–5 Ωcm). Hydrogenated amorphous and nanocrystalline silicon layers were deposited in a radio frequency plasma-enhanced chemical vapour deposition (RF-PECVD) cluster tool manufactured by Applied Materials (AKT1600). Intrinsic a-Si:H passivation layers feature a thickness of 5 nm, doped a-Si:H/nc-Si:H layers approximately 15 nm. The ITO layers (150 nm rear, 20 nm for interconnection layer on front of the IBC cell) were RF-sputtered from a ceramic target with 0.1% oxygen in the Ar/O_2 sputter gas mixture. Ag layers for the IBC rear contacts were deposited with a thickness of 1.5 µm by thermal evaporation. All wafers were annealed at 200 °C for 10 minutes prior to the perovskite processing.

All IBC related layers were patterned using photolithography. Etching the doped a-Si:H/nc-Si:H layers always entails etching the underlying intrinsic a-Si:H layers as well, making a repassivation necessary. To ensure passivation across the whole wafer, the n-type back surface field (BSF) structure overlaps the p-type emitter with a 15 µm margin. The p-type emitter layer (deposited first) was etched with an acidic solution, the n-type BSF layer with an alkaline solution. The latter etches intrinsic and n-type a-Si:H/nc-Si:H at a much faster rate than any p-type material, thus leaving the underlying and already structured emitter layer practically unharmed during the BSF patterning. The total metallisation gap

amounts to 30 µm. The cell area is 1 cm², not including the busbars (designated illumination area, da). Further details can be found in ref [47].

After the IBC processing, individual cells are laser cut to form wafer pieces of roughly (2.5 × 2.5) cm^2, and the perovskite top cells are fabricated on these pieces. For the opaque and semitransparent perovskite reference cell, glass substrates coated with patterned ITO (R = 15 Ω/sq., Automatic Research) were subsequently cleaned for 15 min with acetone, Mucasol detergent (Schülke & Mayr, 2%$_{vol}$ in deionised (DI) H_2O), DI H_2O and isopropyl alcohol (IPA) in an ultrasonic bath. The IBC SHJ bottom cell substrates were only rinsed in IPA to prevent possible delamination of grid fingers through the ultrasonic bath. Afterwards, all samples were transferred to an UV-ozone cleaner and treated for 30 min.

An 0.1 M $SnCl_2 \cdot 2H_2O$ (Sigma Aldrich) solution in ethanol (Honeywell) was deposited to obtain the SnO_2 layer. For this, 70 µl of the solution were dripped onto the samples and then spincoated for 30 s at 1500 rpm (666 rpm/s ramp), followed by spincoating of another 70 µl of the same solution for 30 s at 2500 rpm (666 rpm/s ramp). Afterwards, the samples were annealed at 180°C. Subsequently, the SnO_2 was subjected to another UV-ozone treatment for 15 min and its surface was functionalised by spincoating KNO_3 (2.5 mg/mL, 4000 rpm for 30 s) from aqueous solution and baking for 10 min at 100°C[60]. Further processing was performed in a nitrogen filled glovebox. $Cs_{0.05}(FA_{0.83}MA_{0.17})_{0.95}Pb(I_{0.83}Br_{0.17})_3$ perovskite was prepared following Saliba *et al.*[43] by mixing precursor solutions containing Formamidinium Iodide (FAI, Dyenamo) and Lead Iodide (PbI_2, TCI) with a precursor solution containing Methylammonium Bromide (MABr, Dyenamo) and Lead Bromide ($PbBr_2$, TCI) in the ratio of 5:1. The precursor contained 1 M of the organic and 1.1 M of the lead salts and was dissolved in anhydrous DMF:DMSO 4:1 (vol:vol) which was purchased from Sigma Aldrich. Further on, 5%$_{vol}$ Cesium Iodide (CsI, abcr) from a 1.5 M stock solution in DMSO was added to the precursor solution. It was then spincoated onto the substrates in a two-step programme at 1000 rpm for 10 s and 6000 rpm for 20 s. 5 s prior to the end of the programme, 150 µL of Chlorobenzene (CBZ) was poured on the spinning substrate. Subsequently, the samples were annealed at 120 °C for 1 h. For the HTL, 36.2 mg Spiro-OMeTAD (Sigma) was dissolved in 1 mL of CBZ and then mixed with 14.4 µL 4-tert Butylpyridine (Sigma), 8.8 µL Li-TFSI (Sigma, 520 mg/mL in Acetonitrile (ACN, Sigma)) and 14.5 µL FK209 (Dyenamo, 300 mg/mL M in ACN) and then for 30 s spincoated at 1800 rpm. To protect

the Spiro-OMeTAD layer from sputter damage, 30 nm of MoO_3 (Sigma) was thermally evaporated at a base pressure of 10^{-6} mbar. Subsequently, IZO as a semitransparent front contact was deposited by an RF sputter process similar to that of the IBC SHJ bottom cells' ITO as introduced above. Then, a 150 nm thick layer of silver which was thermally evaporated at a base pressure of 10^{-6} mbar and a rate of 1.2 Å/s. The IBC 3T devices were finished by a 115 nm thick layer of LiF which was thermally evaporated at a base pressure of 10^{-6} mbar and acting as an antireflective coating. Shadow masks were used to define the area of the contact, a busbar surrounding the cell area, thereby defining the designated illumination of 0.78 cm².

Employed Equipment

The current density–voltage (J–V) measurements were performed under standard test conditions (cell temperature 25 °C, LED sun simulator Wavelabs Sinus 70, class AAA), adjusted with a filtered calibrated silicon reference cell (Fraunhofer ISE). The scan rate was 0.333 Vs^{-1} with a voltage step of 20 mV. A mask with an aperture of (9 × 9) mm² was used to selectively reveal the designated illumination area of the cell. For the MPP measurements, we use a dynamic readjustment algorithm which tracks and therefore allows to measure both subcells at their MPP under 3T working conditions. The EQE was measured as a function of wavelength from 340 to 1200 nm with a step of 20 nm using a home built large spot EQE system. The cell was again masked to its designated illumination area as the beam size was exceeding said cell area. When measuring the perovskite top cell, an additional red LED ($\lambda > 850$ nm) could be used as a bias illumination for the silicon bottom cell. For the IBC SHJ with a low photoresponse under low illumination, a white light halogen lamp was used as bias illumination and the such generated photocurrent was compensated with a Keithley 2400 source meter. The reflection measurements were conducted using an integrating sphere with a Perkin Elmer Lambda – 1050 UV/vis/NIR spectrophotometer. The spectrum was measured as a function of wavelength from 300 to 1200 nm with an increment of 2 nm. The instrument was calibrated with a white Spectralon reflection standard.

Supporting Information

J-V-characteristics of the IBC-SHJ before perovskite processing, J-V-characteristics of perovskite single junction reference cells, Further Information on Simulations: Detailed Balanced, Sentaurus TCAD, Optical Simulations, LTspice.

Author Contributions

P.W. and J.C.S. developed the IBC SHJ related processes and P.W. processed the IBC SHJ. P.T. and L.Ke. developed the perovskite-related processes and P.T. processed the IBC 3T devices. P.T., P.W., and L.Ke. conducted the optoelectronic measurements on the IBC 3T devices. J.C.S. and P.T. performed the Sentaurus TCAD and L.Ke. and P.T. the GenPro4 simulations. P.W. conducted the LTspice simulations. M.M. initiated the project. S.A. and L.Ko. supervised the project. P.T., P.W. and J.C.S. wrote the initial manuscript. All authors participated in discussions of the device structure and measurements, in proofreading the manuscript, and correcting it.

Declaration of Interests

The authors declare no competing interests.

Acknowledgement

The authors thank their colleagues from Institute of Silicon Photovoltaics: Alvaro Tejada Esteves for SEM micrographs, Kerstin Jacob and Mona Wittig for RCA cleaning of the wafers, Ganna Chistiakova for O_2 plasma treatment of the SnO_2 layers, and Engin Özkol for depositing the used ITO layers. Furthermore, the HZB institutes EMIL and PVcomB are recognised for equipment as well as the support from Carola Ferber, Monika Gabernig and Hagen Heinz in the HySPRINT lab. The authors acknowledge funding provided by the German Federal Ministry for Education and Research (BMBF, grant no. 03SF0540), the German Federal Ministry for Economic Affairs (BMWi) through the „PersiST“ project (grant no. 0324037C), the HyperCells Graduate School and the HySPRINT Helmholtz Innovation Lab. Philipp Wagner also acknowledges financial support by the HTW Berlin in the framework of the programme ‘HTW Booster’.

References

[1] Philipps S., Warmuth W., Photovoltaics Report - Fraunhofer ISE, 2018

[2] Shockley W., Queisser H.J., Detailed balance limit of efficiency of p-n junction solar cells, J. Appl. Phys., 1961, 32, 510–519

[3] Schafer S., Brendel R., Accurate Calculation of the Absorptance Enhances Efficiency Limit of Crystalline Silicon Solar Cells With Lambertian Light Trapping, IEEE J. Photovoltaics, 2018, 8, 1156–1158

[4] Green M.A., Hishikawa Y., Dunlop E.D., Levi D.H., Hohl-Ebinger J., Yoshita M., Ho-Baillie A.W.Y., Solar cell efficiency tables (Version 53), Prog. Photovoltaics Res. Appl., 2019, 27, 3–12

[5] Yoshikawa K., Kawasaki H., Yoshida W., Irie T., Konishi K., Nakano K., Uto T., Adachi D., Kanematsu M., Uzu H., Yamamoto K., Silicon heterojunction solar cell with interdigitated back contacts for a photoconversion efficiency over 26%, Nat. Energy, 2017, 2, 17032

[6] Dimroth F., Grave M., Beutel P., Fiedeler U., Karcher C., Tibbits T.N.D., Oliva E., Siefer G., Schachtner M., Wekkeli A., Bett A.W., Krause R., Piccin M., Blanc N., Drazek C., Guiot E., Ghyselen B., Salvetat T., Tauzin A., Signamarcheix T., Dobrich A., Hannappel T., Schwarzburg K., Wafer bonded four-junction GaInP/GaAs//GaInAsP/GaInAs concentrator solar cells with 44.7% efficiency, Prog. Photovoltaics Res. Appl., 2014, 22, 277–282

[7] Takamoto T., Washio H., Juso H., Application of InGaP/GaAs/InGaAs triple junction solar cells to space use and concentrator photovoltaic, In: 2014 IEEE 40th Photovoltaic Specialist Conference (PVSC), IEEE, 2014, 0001–0005

[8] Chiu P.T., Law D.., Woo R.L., Singer S.B., Bhusari D., Hong W.D., Zakaria A., Boisvert J., Mesropian S., King R.R., Karam N.H., 35.8% space and 38.8% terrestrial 5J direct bonded cells, In: 2014 IEEE 40th Photovoltaic Specialist Conference (PVSC), IEEE, 2014, 0011–0013

[9] Sasaki K., Agui T., Nakaido K., Takahashi N., Onitsuka R., Takamoto T., Development of InGaP/GaAs/InGaAs inverted triple junction concentrator solar cells, In: AIP Conference Proceedings, American Institute of Physics, 2013, 22–25

[10] Bobela D.C., Gedvilas L., Woodhouse M., Horowitz K.A.W., Basore P.A., Economic competitiveness of III-V on silicon tandem one-sun photovoltaic solar modules in favorable future scenarios, Prog. Photovoltaics Res. Appl., 2017, 25, 41–48

[11] NREL, Best Research-Cell Efficiencies, https://www.nrel.gov/pv/cell-efficiency.html, 2019-11-06.

[12] Vos A. De, Detailed balance limit of the efficiency of tandem solar cells, J. Phys. D. Appl. Phys., 1980, 13, 839–846

[13] Jeon N.J., Na H., Jung E.H., Yang T.-Y., Lee Y.G., Kim G., Shin H.-W., Il Seok S., Lee J., Seo J., A fluorene-terminated hole-transporting material for highly efficient and stable perovskite solar cells, Nat. Energy, 2018, 3, 682–689

[14] Saliba M., Matsui T., Domanski K., Seo J.-Y., Ummadisingu A., Zakeeruddin S.M., Correa-Baena J.-P., Tress W.R., Abate A., Hagfeldt A., Grätzel M., Incorporation of rubidium cations into perovskite solar cells improves photovoltaic performance, Science (80-.)., 2016, 354

[15] Chen B., Yu Z., Liu K., Zheng X., Liu Y., Shi J., Spronk D., Rudd P.N., Holman Z., Huang J., Grain Engineering for Perovskite/Silicon Monolithic Tandem Solar Cells with Efficiency of 25.4%, Joule, 2018

[16] Jošt M., Köhnen E., Morales-Vilches A.B., Lipovšek B., Jäger K., Macco B., Al-Ashouri A., Krč J., Korte L., Rech B., Schlatmann R., Topič M., Stannowski B., Albrecht S., Textured interfaces in monolithic perovskite/silicon tandem solar cells: advanced light management for

improved efficiency and energy yield, Energy Environ. Sci., 2018

[17] Sahli F., Werner J., Kamino B.A., Bräuninger M., Monnard R., Paviet-Salomon B., Barraud L., Ding L., Diaz Leon J.J., Sacchetto D., Cattaneo G., Despeisse M., Boccard M., Nicolay S., Jeangros Q., Niesen B., Ballif C., Fully textured monolithic perovskite/silicon tandem solar cells with 25.2% power conversion efficiency, Nat. Mater., 2018, 17, 820–826

[18] https://www.oxfordpv.com/news/oxford-pv-perovskite-solar-cell-achieves-28-efficiency, n.d.

[19] Köhnen E., Jošt M., Morales-Vilches A.B., Tockhorn P., Al-Ashouri A., Macco B., Kegelmann L., Korte L., Rech B., Schlatmann R., Stannowski B., Albrecht S., Highly efficient monolithic perovskite silicon tandem solar cells: analyzing the influence of current mismatch on device performance, Sustain. Energy Fuels, 2019

[20] Ramírez Quiroz C.O., Shen Y., Salvador M., Forberich K., Schrenker N., Spyropoulos G.D., Heumüller T., Wilkinson B., Kirchartz T., Spiecker E., Verlinden P.J., Zhang X., Green M.A., Ho-Baillie A., Brabec C.J., Balancing electrical and optical losses for efficient 4-terminal Si–perovskite solar cells with solution processed percolation electrodes, J. Mater. Chem. A, 2018, 6, 3583–3592

[21] Duong T., Wu Y., Shen H., Peng J., Fu X., Jacobs D., Wang E.-C., Kho T.C., Fong K.C., Stocks M., Franklin E., Blakers A., Zin N., McIntosh K., Li W., Cheng Y.-B., White T.P., Weber K., Catchpole K., Rubidium Multication Perovskite with Optimized Bandgap for Perovskite-Silicon Tandem with over 26% Efficiency, Adv. Energy Mater., 2017, 7, 1700228

[22] Futscher M.H., Ehrler B., Modeling the Performance Limitations and Prospects of Perovskite/Si Tandem Solar Cells under Realistic Operating Conditions, ACS Energy Lett., 2017, 2, 2089–2095

[23] Hörantner M.T., Snaith H.J., Predicting and optimising the energy yield of perovskite-on-silicon tandem solar cells under real world conditions, Energy Environ. Sci., 2017, 10, 1983–1993

[24] Jäger K., Korte L., Rech B., Albrecht S., Numerical optical optimization of monolithic planar perovskite-silicon tandem solar cells with regular and inverted device architectures, Opt. Express, 2017, 25, A473

[25] Santbergen R., Uzu H., Yamamoto K., Zeman M., Optimization of Three-Terminal Perovskite/Silicon Tandem Solar Cells, IEEE J. Photovoltaics, 2019, 1–6

[26] Schnabel M., Rienacker M., Warren E.L., Geisz J.F., Peibst R., Stradins P., Tamboli A.C., Equivalent Performance in Three-Terminal and Four-Terminal Tandem Solar Cells, IEEE J. Photovoltaics, 2018, 1–6

[27] Schulte-Huxel H., Friedman D.J., Tamboli A.C., String-Level Modeling of Two, Three, and Four Terminal Si-Based Tandem Modules, IEEE J. Photovoltaics, 2018, 8, 1370–1375

[28] Sakai S., Umeno M., Theoretical analysis of new wavelength-division solar cells, J. Appl. Phys., 1980, 51, 5018–5024

[29] Ito N., Uesugi T., Sakai S., Umeno M., Hattori S., InGaAsP/InP Wavelength Division Solar Cells, Jpn. J. Appl. Phys., 1981, 20, 121

[30] Soga T., Yang M., Jimbo T., Umeno M., High-Efficiency Monolithic Three-Terminal GaAs/Si Tandem Solar Cells Fabricated by Metalorganic Chemical Vapor Deposition, Jpn. J. Appl. Phys., 1996, 35, 1401–1404

[31] Park I.J., Park J.H., Ji S.G., Park M.-A., Jang J.H., Kim J.Y., A Three-Terminal Monolithic Perovskite/Si Tandem Solar Cell Characterization Platform, Joule, 2018

[32] Nagashima T., Okumura K., Murata K., Kimura Y., Three-terminal tandem solar cells with a back-contact type bottom cell, In: Conference Record of the Twenty-Eighth IEEE Photovoltaic

Specialists Conference - 2000 (Cat. No.00CH37036), IEEE, n.d., 1193–1196

[33] Warren E.L., Deceglie M.G., Rienäcker M., Peibst R., Tamboli A.C., Stradins P., Maximizing tandem solar cell power extraction using a three-terminal design, Sustain. Energy Fuels, 2018, 2, 1141–1147

[34] Djebbour Z., El-Huni W., Migan Dubois A., Kleider J.-P., Bandgap engineered smart three-terminal solar cell: New perspectives towards very high efficiencies in the silicon world, Prog. Photovoltaics Res. Appl., 2019

[35] Schnabel M., Schulte-Huxel H., Rienäcker M., Warren E.L., Ndione P.F., Nemeth W., Klein T.R., van Hest M.F.A.M., Geisz J., Peibst R., Stradins P., Tamboli A.C., Three-Terminal III-V/Si Tandem Solar Cells Enabled by a Transparent Conductive Adhesive, Sustain. Energy Fuels, 2019

[36] Rienäcker M., Warren E.L., Schnabel M., Schulte-Huxel H., Niepelt R., Brendel R., Stradins P., Tamboli A.C., Peibst R., Back-contacted bottom cells with three terminals: Maximizing power extraction from current-mismatched tandem cells, Prog. Photovoltaics Res. Appl., 2019, pip.3107

[37] Adhyaksa G.W.P., Johlin E., Garnett E.C., Nanoscale Back Contact Perovskite Solar Cell Design for Improved Tandem Efficiency, Nano Lett., 2017, 17, 5206–5212

[38] Mazzarella L., Werth M., Jäger K., Jošt M., Korte L., Albrecht S., Schlatmann R., Stannowski B., Infrared photocurrent management in monolithic perovskite/silicon heterojunction tandem solar cells by using a nanocrystalline silicon oxide interlayer, Opt. Express, 2018, 26, A487

[39] Futscher M.H., Ehrler B., Efficiency Limit of Perovskite/Si Tandem Solar Cells, ACS Energy Lett., 2016, 2–7

[40] Wagner P., Stang J.-C., Mews M., Morales-Vilches A.B., Stannowski B., Stegemann B., Korte L., Interdigitated back contact silicon heterojunction solar cells: Towards an industrially applicable structuring method, In: AIP Conference Proceedings, AIP Publishing LLC , 2018, 060001

[41] Chen D., Manley P., Tockhorn P., Eisenhauer D., Köppel G., Hammerschmidt M., Burger S., Albrecht S., Becker C., Jäger K., Nanophotonic light management for perovskite–silicon tandem solar cells, J. Photonics Energy, 2018, 8, 1

[42] Mazzarella L., Morales-Vilches A.B., Hendrichs M., Kirner S., Korte L., Schlatmann R., Stannowski B., Nanocrystalline n-Type Silicon Oxide Front Contacts for Silicon Heterojunction Solar Cells: Photocurrent Enhancement on Planar and Textured Substrates, IEEE J. Photovoltaics, 2018, 8, 70–78

[43] Saliba M., Matsui T., Seo J.-Y., Domanski K., Correa-Baena J.-P., Nazeeruddin M.K., Zakeeruddin S.M., Tress W., Abate A., Hagfeldt A., Grätzel M., Cesium-containing triple cation perovskite solar cells: improved stability, reproducibility and high efficiency, Energy Environ. Sci., 2016, 9, 1989–1997

[44] Löper P., Moon S.-J., Nicolas S.M. de, Niesen B., Ledinsky M., Nicolay S., Bailat J., Yum J.-H., Wolf S. De, Ballif C., Organic–inorganic halide perovskite/crystalline silicon four-terminal tandem solar cells, Phys. Chem. Chem. Phys., 2014, 1619–1629

[45] Green M.A., Emery K., Hishikawa Y., Warta W., Dunlop E.D., Solar cell efficiency tables (version 39), Prog. Photovoltaics Res. Appl., 2012, 20, 12–20

[46] Quaschning V., Hanitsch R., Influence of shading on electrical parameters of solar cells, In: Conference Record of the Twenty Fifth IEEE Photovoltaic Specialists Conference - 1996, IEEE, 1996, 1287–1290

[47] Stang J.-C., Interdigitated back contact silicon heterojunction solar cells: from the laboratory to

industrial processes, PhD Thesis, Tech. Univ. Berlin, 2018

[48] Werner J., Geissbühler J., Dabirian A., Nicolay S., Morales-Masis M., Wolf S. De, Niesen B., Ballif C., Parasitic Absorption Reduction in Metal Oxide-Based Transparent Electrodes: Application in Perovskite Solar Cells, ACS Appl. Mater. Interfaces, 2016, 8, 17260–17267

[49] Albrecht S., Saliba M., Correa Baena J.P., Lang F., Kegelmann L., Mews M., Steier L., Abate A., Rappich J., Korte L., Schlatmann R., Nazeeruddin M.K., Hagfeldt A., Grätzel M., Rech B., Correa-Baena J.-P., Lang F., Kegelmann L., Mews M., Steier L., Abate A., Rappich J., Korte L., Schlatmann R., Nazeeruddin M.K., Hagfeldt A., Grätzel M., Rech B., Monolithic perovskite/silicon-heterojunction tandem solar cells processed at low temperature, Energy Environ. Sci., 2016, 9, 81–88

[50] Santbergen R., Meguro T., Suezaki T., Koizumi G., Yamamoto K., Zeman M., GenPro4 Optical Model for Solar Cell Simulation and Its Application to Multijunction Solar Cells, IEEE J. Photovoltaics, 2017, 7, 919–926

[51] Santbergen R., Smets A.H.M.M., Zeman M., Optical model for multilayer structures with coherent, partly coherent and incoherent layers., Opt. Express, 2013, 21 Suppl 2, A262-7

[52] Wu N., Wu Y., Walter D., Shen H., Duong T., Grant D., Barugkin C., Fu X., Peng J., White T., Catchpole K.R., Weber K., Identifying the Cause of Voltage and Fill Factor Losses in Perovskite Solar Cells by Using Luminescence Measurements, Energy Technol., 2017, 5, 1827–1835

[53] Saliba M., Matsui T., Seo J.-Y., Domanski K., Correa-Baena J.-P., Nazeeruddin M.K., Zakeeruddin S.M., Tress W., Abate A., Hagfeldt A., Grätzel M., Cesium-containing triple cation perovskite solar cells: improved stability, reproducibility and high efficiency, Energy Environ. Sci., 2016, 9, 1989–1997

[54] Nakamura J., Asano N., Hieda T., Okamoto C., Katayama H., Nakamura K., Development of Heterojunction Back Contact Si Solar Cells, IEEE J. Photovoltaics, 2014, 4, 1491–1495

[55] Würfel U., Cuevas A., Würfel P., Charge Carrier Separation in Solar Cells, IEEE J. Photovoltaics, 2015, 5, 461–469

[56] Djebbour Z., El-Huni W., Migan Dubois A., Kleider J., Bandgap engineered smart three-terminal solar cell: New perspectives towards very high efficiencies in the silicon world, Prog. Photovoltaics Res. Appl., 2019, 27, 306–315

[57] Linear Technology, LTspice, https://www.analog.com/en/%0Adesign-center/design-tools-and-calculators/ltspicesimulator.html.%0A, 2019-07-20

[58] Paviet-Salomon B., Tomasi A., Lachenal D., Badel N., Christmann G., Barraud L., Descœudres A., Geissbühler J., Faes A., Jeangros Q., Seif J.P., Nicolay S., Strahm B., De Wolf S., Ballif C., Despeisse M., Interdigitated back contact silicon heterojunction solar cells featuring an interband tunnel junction enabling simplified processing, Sol. Energy, 2018, 175, 60–67

[59] Lee S.-Y., Choi H., Li H., Ji K., Nam S., Choi J., Ahn S.-W., Lee H.-M., Park B., Analysis of a-Si:H/TCO contact resistance for the Si heterojunction back-contact solar cell, Sol. Energy Mater. Sol. Cells, 2014, 120, 412–416

[60] Dagar J., Hirselandt K., Merdasa A., Czudek A., Munir R., Zu F., Koch N., Dittrich T., Unger E.L., Alkali Salts as Interface Modifiers in n-i-p Hybrid Perovskite Solar Cells, Sol. RRL, 2019, 3, 1900088